Generation of shear Alfvén waves by a rotating magnetic field source: 3D Simulations

A. V. Karavaev,* N. A. Gumerov, K. Papadopoulos, Xi Shao, and A. S. Sharma
Department of Physics and Department of Astronomy, University of Maryland, College Park, MD 20742, United States

W. Gekelman, Y. Wang, B. Van Compernolle, P. Pribyl, and S. Vincena
Department of Physics and Astronomy, University of California, Los Angeles, CA 90095, United States

(Dated: August 15, 2010)

The paper discusses the generation of polarized shear Alfvén waves radiated from a rotating magnetic field source created via a phased orthogonal two-loop antenna. A semi-analytical three-dimensional cold two-fluid magnetohydrodynamics model was developed and compared with recent experiments in the UCLA large plasma device. Comparison of the simulation results with the experimental measurements and the linear shear Alfvén wave properties, namely, spatio-temporal wave structure, a dispersion relation with nonzero transverse wave number, the magnitude of the wave dependences on the wave frequency, show good agreement. From the simulations it was found that the energy of the Alfvén wave generated by the rotating magnetic field source is distributed between the kinetic energy of ions and electrons and the electromagnetic energy of the wave as: $\sim 1/2$ is the energy of the electromagnetic field, $\sim 1/2$ is the kinetic energy of the ion fluid, and $\sim 2.5\%$ is the kinetic energy of electron fluid for the experiment. The wave magnetic field power calculated from the experimental data and using a fluid model defer by $\sim 1\%$ and is ~ 250 W for the experimental parameters. In both the experiment and the three-dimensional two-fluid magnetohydrodynamics simulations the rotating magnetic field source was found to be very efficient for generating shear Alfvén waves.

I. INTRODUCTION

Shear Alfvén waves (SAW) have been observed in a number of laboratory experiments[1] and in nature in a wide variety of astrophysical magnetized plasmas such as planetary magnetospheres[2], Earth's aurora[3], solar corona[4], *etc.* Because of its propagation nearly along an ambient magnetic field[5–7], SAW can transport energy efficiently. The SAW can drive plasma currents, and in fact, one may think of almost any low frequency current system in magnetized plasmas as an Alfvénic wave system. The SAW can play a major role in wave particle-acceleration in various magnetized plasma configurations in space[4,8–11].

Although there has been a variety of SAW experiments[1], including generation by a rotating magnetic field source with the frequencies approaching the ion cyclotron frequency Ω_{ci} used for a resonant ion cyclotron heating[12,13], the basic physics of the interaction of rotating magnetic fields (RMF) with magnetized plasmas in a wide frequency range below the ion cyclotron frequency Ω_{ci} remain unexplored. The following experimental and theoretical study of the interaction of the RMF with magnetized plasma addresses the spatio-temporal structure, properties of the propagation and the dispersion relation of the induced waves as a function of the RMF and plasma parameters.

The interest in the generation of SAW by the RMF sources arise in many settings, *e.g.*, their possible applications to the controlled electron radiation belt remediation in the inner Van Allen belt. The SAWs generated by a RMF source can create in the inner radiation belt a non-local magnetic field gradient, which can lead to non-resonant breaking of the adiabatic invariant $\mu = v_\perp^2/B$ for the trapped electrons, and their pitch-angle scattering into the loss cone.

Recently experiments on the generation of whistler[14] and shear Alfvén waves[15] by a RMF source were performed on the Large Plasma Device (LAPD)[16] at the University of California, Los Angeles. These experiments highlighted the properties of RMF antennas as efficient sources of waves in plasmas in a broad frequency range. The detailed description of the experimental setup and the RMF radiation source for whistler and shear Alfvén waves regimes can be found in Refs.[14,15].

The main focus of the present paper is the development of a 3D simulation model of the shear Alfvén waves generated by the RMF source and the comparison of the results with the experiments. The good agreement of the 3D model with the experimental results suggests its predictive capability.

II. EXPERIMENTS ON THE GENERATION SHEAR ALFVÉN WAVES BY RMF

Two sets of the experiments on the generation of SAW by the RMF source were performed on the LAPD, and the general plasma parameters are presented in Table I. The first experiment[15] was mainly focused on the measurements of the spatio-temporal structure of SAW generated by the RMF source. In that experiment the three components of the perturbed magnetic field were measured in planes perpendicular to the ambient magnetic field at different z-locations, which provided three-dimensional volumetric data of the wave magnetic field and current structures over the course of ~ 2.5 parallel

wavelength of the SAW for the frequency $\omega = 0.54\Omega_{ci}$. The main goal of the second set of experiments was a measurement of the dependences of the generated wave parameters on the driving frequency while the other parameters of the experiment were kept constant. The major difference between the plasma parameters in two experiments is that in the second setup the plasma density was lower ($n = 1.3 \times 10^{12} cm^{-3}$ compared to $n = 2.3 \times 10^{12} cm^{-3}$ in the first setup), and the electrons were colder ($T_e = 1.5\ eV$ compared to $T_e = 6\ eV$). As a result we measured higher values of wave magnitudes at the same locations and for the same input current parameters in the second experiment than in the first one.

The RMF source used in the experiments is a phased, orthogonal two loop antenna. The antenna is composed of two independent coils of 0.25 *cm* diameter solid copper wire with three turns each. The diameter of the coils are roughly 8 *cm* and 9 *cm*, which are ~ 23 and ~ 26 electron skin-depth $\lambda_e = c/\omega_{pe}$ for the first experimental set. The coils are driven by two independent high power resonant LRC circuits utilizing the inductance of the antenna and the inherent line resistance, whose resonance frequencies can be adjusted with the capacitance in a matched circuit, set $\pm 90^o$ out of phase so that the total magnetic moment generated by the two coils had left-handed or right-handed circular polarization. The antenna is oriented in such a way that its center is located on the symmetry axis of the LAPD-machine, and one of the loops lies in the xz-plane, while the second lays in the yz-plane. The coordinate system is defined with z-axis along the ambient magnetic field (the central axis of the machine) and y-axis pointing upwards. The driving frequency used in the experiment was in the range $80 - 355\ kHz$ ($0.21 - 0.93\Omega_{ci}$). The magnitude of the current in the coils was up to $\sim 600\ Amps$.

The primary diagnostic used in the experiment is a three-axis magnetic pickup coil[19]. The probe features differentially wound loops that eliminate electrostatic pickup when used in conjunction with a differential amplifier. The loops of the probe are wound around 1 *mm* cube with ten turns each. The cube is mounted within a glass tube and attached to a thin ceramic tube extending from the end of a stainless steel probe shaft. Using a computer controlled data acquisition system the measurements of the three components of perturbed magnetic field on a square area 41×41 points with 0.75 *cm* spacing at several cross sectional planes perpendicular to the ambient magnetic field were performed for different driving frequencies and polarizations of the RMF source.

III. COMPARISON OF TWO-FLUID MHD MODEL AND EXPERIMENT

A. Magnetic field structure

In the experiments it was found that the RMF source is capable of driving relatively large magnitude field shear Alfvén waves with the peak amplitudes up to a couple of tens of *Gauss* for input current magnitudes 600 *Amps* with polarization depending on that of the RMF source. Although the wave field magnitudes were ~ 10 *Gauss* (a large magnitude for Alfvén waves produced in the LAPD) in absolute value, they are only 1 % of the background magnetic field B_0, which is natural magnetic field scale of the problem. It has been shown[20] that large enough amplitude SAWs can lead to wave current filamentation and modification of the plasma density due to the ponderomotive force. However, in order for this nonlinear effect to be important the wave magnitude should be of order 10 % or higher of the background magnetic field[20]. In our case of ~ 1 % magnetic field perturbations a linear approximation should work fairly well in the wide range of frequencies except the narrow frequency regions around resonances, for example, at the ion cyclotron frequency, where ion cyclotron resonance heating starts to play an important role.

A three-dimensional (3D) two-fluid magnetohydrodynamics (MHD) code, described in detail in the Appendix, was developed and implemented using the MATLAB environment to simulate the experiments with the parameters presented in Table I and a variable driving frequency. A typical mesh of $180 \times 180 \times 1000$ (32.4×10^6) grid points varying linear sizes of the computational domain was used in the simulations of Alfvén waves generated by the RMF source.

In both the experiments and 3D simulations the observed wave magnetic field generated by the RMF antenna lies primarily in the plane perpendicular to the ambient magnetic field (the magnitudes $B_x \approx B_y \gg B_z$). In the 3D simulations we found that the wave electric field is nearly normal to both the background magnetic field and the magnetic field perturbation. The wave electric field component perpendicular to the ambient magnetic field is much bigger than the parallel (the magnitudes $E_x \approx E_y \sim 100 E_z$), which is consistent with the properties of the SAWs[5–7] radiated from a source with small transverse size (that is high perpendicular wave number $k_\perp$)[21].

Figures 1, 2, and 3 show the magnetic field structures in one of the planes perpendicular to the ambient magnetic field measured in the experiment (Experiment set 2) and calculated using 3D two-fluid MHD model for different polarizations of the radiation source. The ambient magnetic field points outwards of the plane of the figures.

In Fig. 1(a.1)-(a.4) the perturbed magnetic field structure measured in the experiment for left-handed polarization of the RMF source at the plane $z = 2.88\ m$ away from the antenna for four different instants of time separated by 1/4 of the wave period (driving frequency $f_d = 80\ kHz$) are presented. Fig. 1(b.1)-(b.4) show the same plane magnetic field for the same time instants calculated from the 3D two-fluid MHD model. As the time goes (from left to right) the magnetic field in the plane rotates clockwise around the ambient magnetic field.

Fig. 2(a.1)-(a.4) show the perturbed magnetic field

TABLE I: Parameters of the experiments on generating SAW by the RMF source.

Parameter	Experiment set 1[15]	Experiment set 2
Ions	He^+	He^+
Gas pressure	$\sim 10^{-4}$ *Torr*	$\sim 10^{-4}$ *Torr*
Ambient magnetic field	10^3 *Gauss*	10^3 *Gauss*
Plasma density	$2.3 \pm 0.3 \times 10^{12} cm^{-3}$	$1.3 \pm 0.2 \times 10^{12} cm^{-3}$
(microwave interferometer)		
Electron temperature	6 ± 1 *eV*	1.5 ± 0.5 *eV*
Ion temperature	1 ± 0.5 *eV*	0.5 ± 0.3 *eV*
(Langmuir probe)		
Electron plasma frequency	$8.6 \times 10^{10} s^{-1}$	$6.4 \times 10^{10} s^{-1}$
Electron skin-depth	3.5 *mm*	4.7 *mm*
Electron cyclotron frequency	$1.76 \times 10^{10} s^{-1}$	$1.76 \times 10^{10} s^{-1}$
Ion cyclotron frequency	$2.4 \times 10^6 s^{-1}$	$2.4 \times 10^6 s^{-1}$
Electron-neutral collision frequency[17]	$2.8 \pm 0.2 \times 10^5 s^{-1}$	$8.9 \pm 0.1 \times 10^4 s^{-1}$
Ion-neutral collision frequency	$\sim 10^2 s^{-1}$	$\sim 10^2 s^{-1}$
Coulomb collision frequency[18]	$4.75 \pm 1.15 \times 10^6 s^{-1}$	$1.75 \pm 0.4 \times 10^7 s^{-1}$

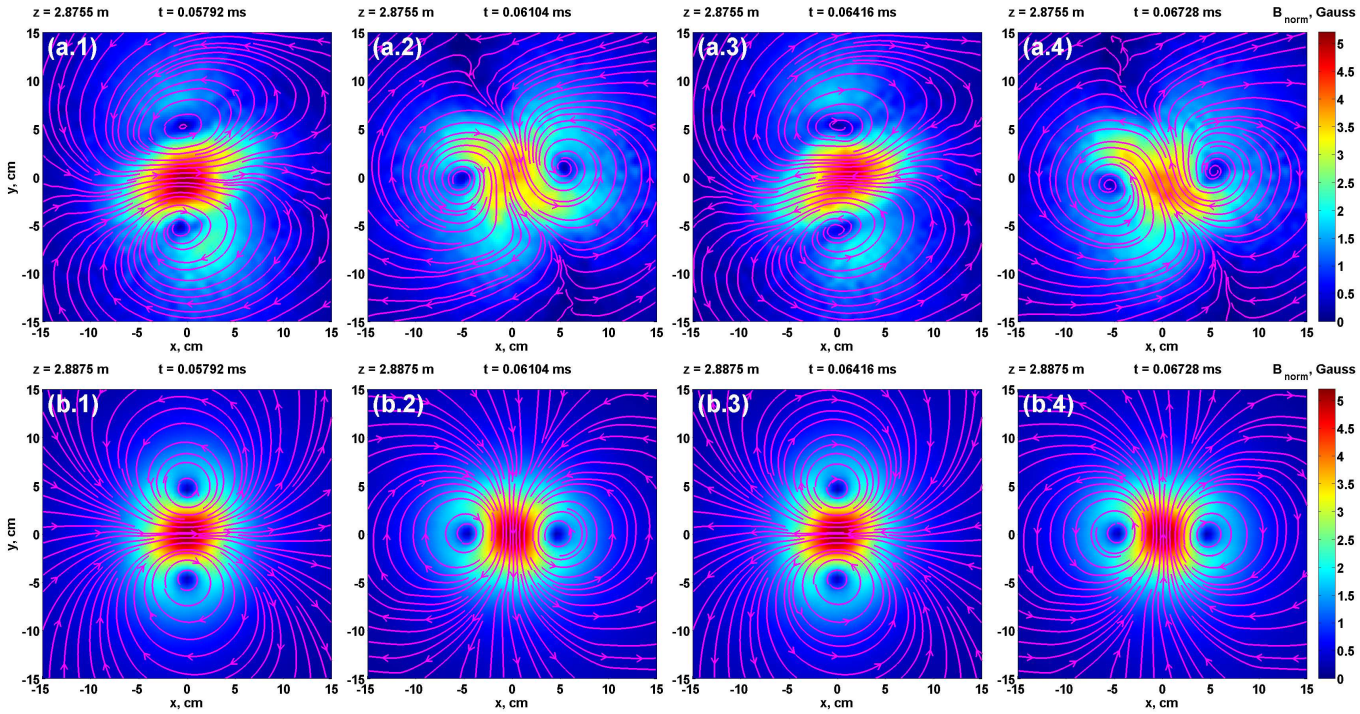

FIG. 1: (Color online) Comparison of the magnetic field structure in the plane $z = 2.88$ *m* away from the radiating antenna for four instants of time ($t_1 = 0.05792$ *ms*, $t_2 = 0.06104$ *ms*, $t_3 = 0.06416$ *ms*, and $t_4 = 0.06728$ *ms* from the beginning of the pulse) separated by 1/4 of the wave period (driving frequency $f_d = 80$ *kHz*) measured in the experiment (Experiment set 2) ((a.1) - (a.4)) and calculated using 3D model ((b.1) - (b.4)) for the left-handed polarization case. The ambient magnetic field $B_0 = 1000$ *Gauss* points outward of the plane of the picture.

structure measured in the experiment for case of a one-loop antenna (the current laying in the $x - z$-plane was turned off) for four different instants of time. Fig. 2(b.1)-(b.4) show the magnetic field in the same plane for the same times as in Fig. 2(a.1)-(a.4) from the simulations. The magnetic field perturbation has nearly linear polarization in this case, and as the time progresses (from left to right) the magnetic field in the center of the plane oscillates in the x-direction.

Figure 3 is similar to Figs. 1, 2 graphs except the polarization of the RMF source was set to be right-handed. In this case the magnetic field rotates counterclockwise around z-axis. One can see good agreement of the 3D simulations and the experiment for all the cases. Note also a good agreement of the phase between the model and the experiment, which confirms that parallel phase

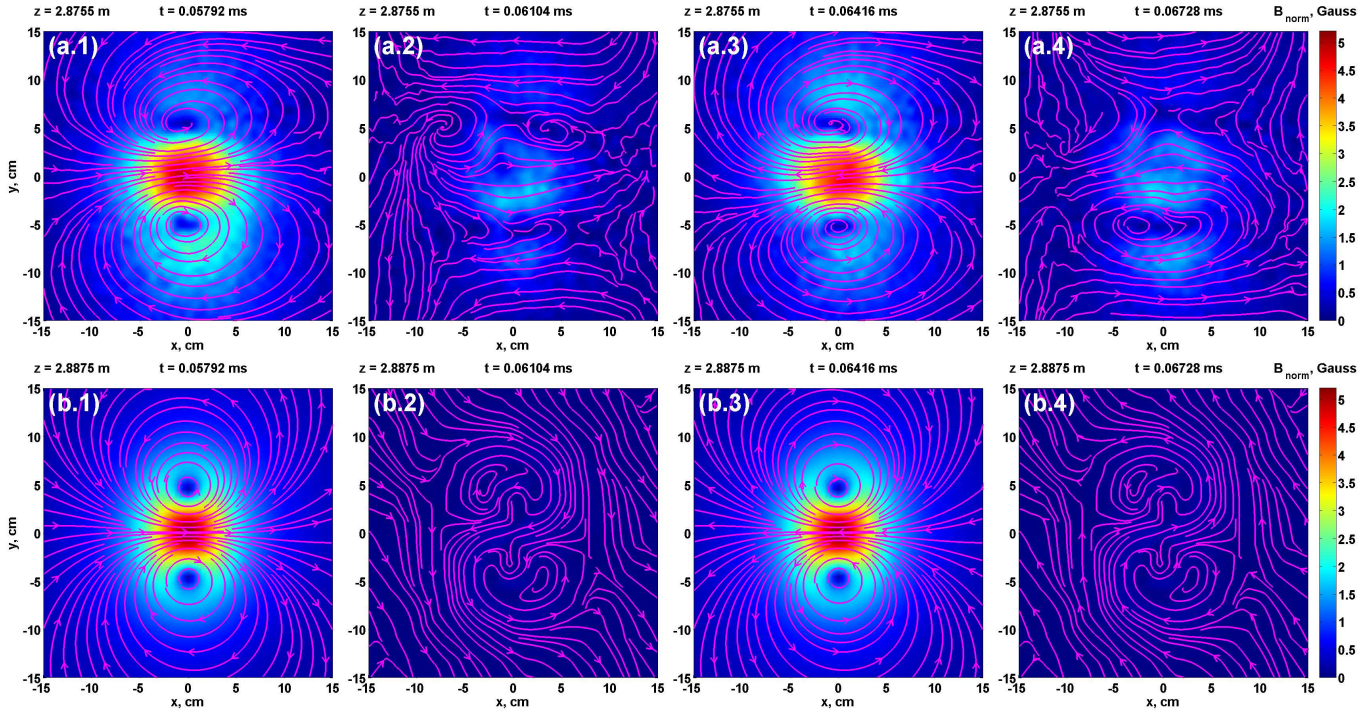

FIG. 2: (Color online) Comparison of the magnetic field structure in the plane $z = 2.88\ m$ away from the radiating antenna for four instants of time ($t_1 = 0.05792\ ms$, $t_2 = 0.06104\ ms$, $t_3 = 0.06416\ ms$, and $t_4 = 0.06728\ ms$ from the beginning of the pulse) separated by 1/4 of the wave period (driving frequency $f_d = 80\ kHz$) measured in the experiment (Experiment set 2) ((a.1) - (a.4)) and calculated using 3D model ((b.1) - (b.4)) for single loop antenna case. The antenna loop in the xz-plane is turned off. The ambient magnetic field $B_0 = 1000\ Gauss$ points outwards of the plane of the picture.

velocities in the experiment and the simulations are very close.

The magnitude of the perturbed magnetic field has its maximum in the center of the plane, that is on the symmetry axis of the machine, for all cases. The maximum of the magnitude is found to be independent of the polarization of the RMF source and on whether one or two loops are used. The characteristic transverse size of the wave propagating along the ambient magnetic field is about 20 cm in extent, which is approximately twice the diameter of the antenna loops, does not depend on the frequency or the distance from the antenna along the z-axis. One more feature of the magnetic field structure is the two vortex structure with nearly constant distance between the centers of these vortices $\sim 9\ cm$, which is determined by the antenna size. Using $\boldsymbol{\nabla} \times \mathbf{B} = 4\pi/c\mathbf{J}$, the centers of the vortices are found to correspond to the maxima of field aligned currents. This is similar to a pattern observed of Alfvén waves produced by two oscillating current channels and with a helical antenna[22,23].

Figure 4 shows the dependence of the magnitude of wave magnetic field along the ambient magnetic field measured in the experiment (Experiment set 1) - diamonds with uncertainty margins, approximation of the experimental data by the exponentially decaying function $A\exp(-k_i z)$ (A is the magnitude at $z = 0$, and k_i is imaginary part of the longitudinal wave number $k_{||}$) - dashed line, calculated in the 3D simulations - solid line, and calculated using analytical dispersion relation Eq. (1) - dash-dotted line for left-handed polarization of the RMF and driving frequency $f_d = 206\ kHz \sim 0.54 f_{ci}$. All of the curves shown exhibit an exponential decay with the rates $k_i = 0.101\ m^{-1}$ for the experiment, $k_i = 0.106\ m^{-1}$ for the model and $k_i = 0.083\ m^{-1}$ for the analytical dispersion relation, respectively, which are very close.

Figure 5 shows the dependence of the wave magnetic field magnitude as a function of the transverse coordinate x for four different locations along z-axis calculated using the 3D model and measured in the experiment (Experiment set 1). One can see good quantitative agreement of the 3D model results with the experimental measurements.

B. SAW dispersion relation

The SAW is an electromagnetic mode of magnetized plasmas and propagates nearly parallel to the background magnetic field in the frequency range below the ion cyclotron frequency $\omega < \Omega_{ci}$. For the parameters of the experiment the dispersion relation for the kinetic SAW including the effects of finite frequency and colli-

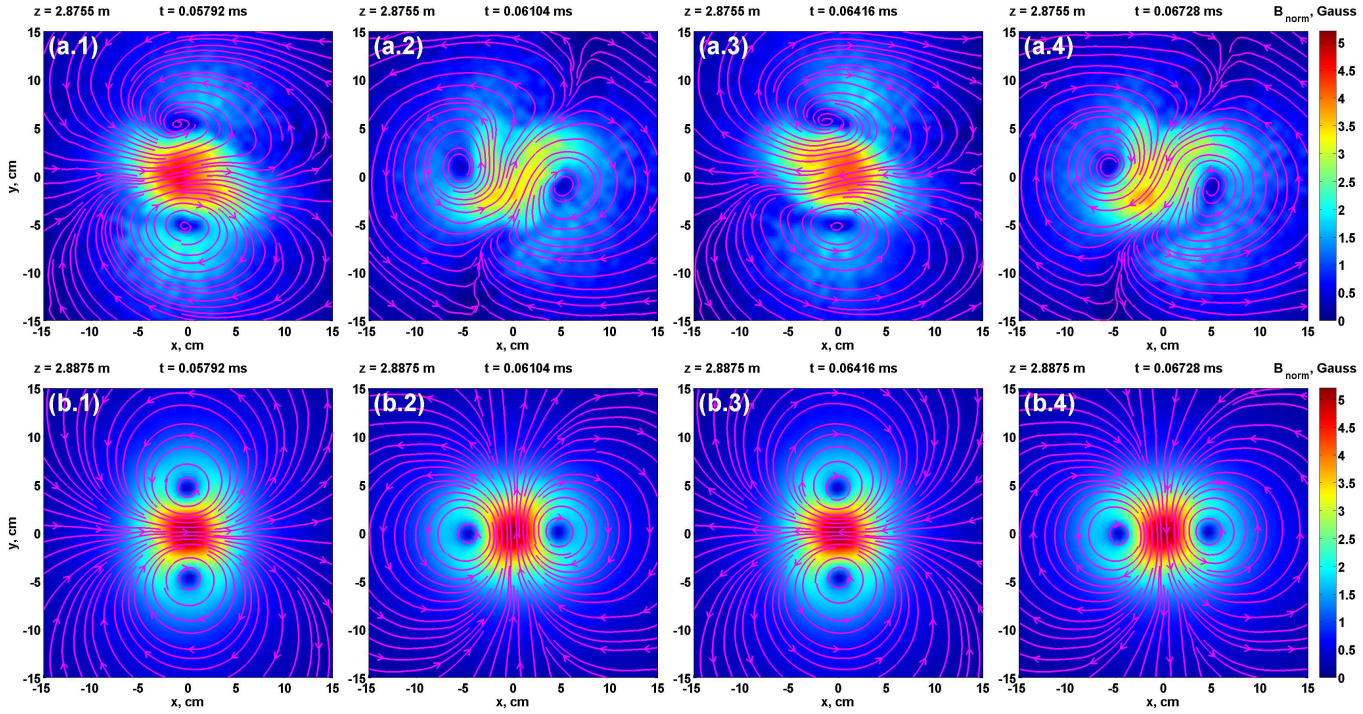

FIG. 3: (Color online) Comparison of the magnetic field structure in the plane $z = 2.88\ m$ away from the radiating antenna for four instants of time ($t_1 = 0.05792\ ms$, $t_2 = 0.06104\ ms$, $t_3 = 0.06416\ ms$, and $t_4 = 0.06728\ ms$ from the beginning of the pulse) separated by 1/4 of the wave period (driving frequency $f_d = 80\ kHz$) measured in the experiment (Experiment set 2) ((a.1) - (a.4)) and calculated using 3D model ((b.1) - (b.4)) for the right-handed polarization case. The ambient magnetic field $B_0 = 1000\ Gauss$ points outwards from the plane of the picture.

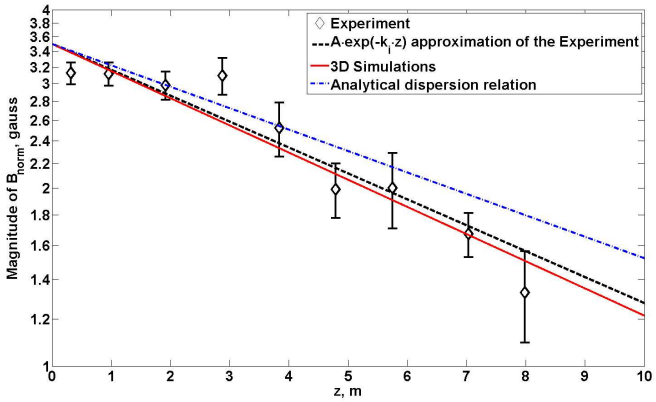

FIG. 4: (Color online) Dependence of the magnitude of perturbed magnetic field on distance z from the radiating antenna along the ambient magnetic field measured in the experiment (Experiment set 1) and calculated using 3D model. The amplitude dependence predicted by analytical dispersion relation Eq. (1) is plotted as well. Driving frequency $\omega = 0.54\Omega_{ci}$, left-handed polarization of the RMF.

sions can be written as[24]

$$\omega^2 - k_{||}^2 V_A^2 \left(1 - \frac{\omega^2}{\Omega_{ci}} + (\rho_s k_\perp)^2\right) + i\omega\nu_e k_\perp^2 \lambda_e^2 = 0, \quad (1)$$

where $\lambda_e = c/\omega_{pe}$ is the electron skin-depth, $\rho_s = c_s/\Omega_{ci}$ is the ion sound gyroradius, $c_s = (T_e/m_i)^{1/2}$ is the sound speed, T_e is the electron temperature, $k_\perp$ and $k_{||}$ are wave vector components perpendicular and parallel to the ambient magnetic field, $V_A = B_0/(4\pi n_i m_i)^{1/2}$ is the Alfvén speed, and ν_e is the effective electron collision frequency. In general, the propagation of the SAW across the ambient magnetic field is much slower than along the ambient field ($v_{ph\perp} = \omega/k_\perp \ll v_{ph||} = \omega/k_{||}$)[21,25,26] especially for the case when the wave is generated by a source with small transverse size. As a result, the SAW is within a fixed flux tube containing the source.

Introducing the angle θ between the direction of the wave vector $\mathbf{k}$ and ambient magnetic field we can write $k_\perp = k\sin\theta$ and $k_{||} = k\cos\theta$, where k is the magnitude of the wave vector. Substituting $k_\perp$ and $k_{||}$ into Eq. (1) we can solve it for k as a function of ω and θ as

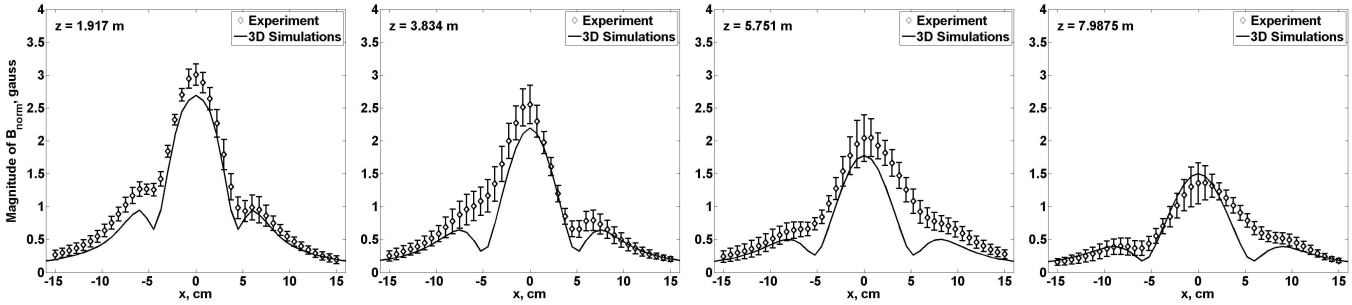

FIG. 5: Dependence of the magnitude of perturbed magnetic field on x-coordinate perpendicular to the ambient magnetic field for different cross sections ($z = 1.917\ m$, $z = 3.834\ m$, $z = 5.751\ m$, and $z = 7.9875\ m$) measured in the experiment (Experiment set 1) and calculated using 3D model. Driving frequency $\omega = 0.54\Omega_{ci}$, left-handed polarization of the RMF.

$$k_{1,2}^2 = \frac{i\frac{\omega\nu_e\lambda_e^2}{V_A^2}\tan^2\theta - \left(1-\frac{\omega^2}{\Omega_{ci}^2}\right) \pm \sqrt{\left(i\frac{\omega\nu_e\lambda_e^2}{V_A^2}\tan^2\theta - \left(1-\frac{\omega^2}{\Omega_{ci}^2}\right)\right)^2 + 4\frac{\omega^2\rho_s^2}{V_A^2}\tan^2\theta}}{2\rho_s^2\sin^2\theta} \tag{2}$$

In Fig. 6 the dependences between the perpendicular $k_\perp$ and parallel $k_{||}$ wave numbers calculated using Eq. (2) for collisional and collisionless cases, and those obtained from the numerical solution of 3D model are presented for the driving frequency $\omega = 0.54\Omega_{ci}$. The parallel wave numbers corresponding to the parallel phase velocity measured in the experiment are represented by two vertical dashed lines. The general features of the curves calculated from Eq. (2) and obtained numerically using the 3D model are very similar, in particular close to each other in the region of interest.

In Fig. 7 the dispersion relation ($k_{||}$ as a function of ω) is presented. Solid curves represent the dispersion relation found using the 3D model for collisionless ($\square$) and finite collision ($\circ$) cases. The dashed line represents the $k_{||}$ on ω dependence found using Eq. (1) assuming $Re\,(\lambda_\perp) = 18\ cm$. The symbols with uncertainty margins represent experimental measurements. One can see good qualitative agreement of the theory, simulations and the experiment, although the difference between the experiment and the 3D model predictions becomes significant for the higher frequencies approaching the ion cyclotron frequency.

In Fig. 8 the dependence of parallel phase velocity on frequency found using 3D model, calculated from Eq. (1) and measured in the experiment is presented. There is good agreement between them.

C. 3D plasma current structure

Using the 3D two-fluid MHD model we found the plasma current structure for the parameters of the experiment (See Table I) and driving frequency $f_d = 0.54\Omega_{ci}$.

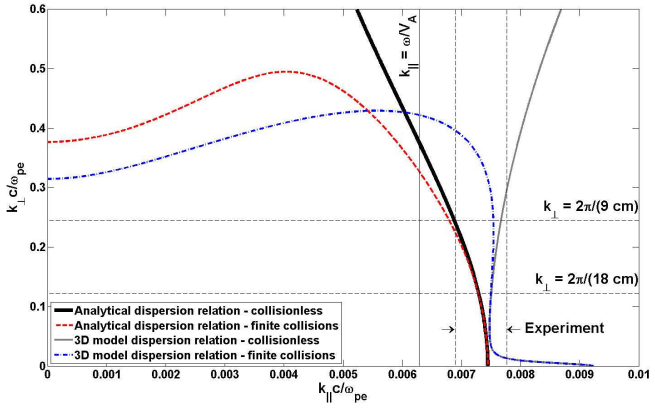

FIG. 6: (Color online) Dependence of transverse wave number $k_\perp$ on the longitudinal wave number $k_{||}$ for frequency $\omega = 0.54\Omega_{ci}$ given by analytical dispersion relation (Eq. (1)) and embedded in the 3D model for collisionless and collisional cases. The longitudinal wave number $k_{||}$ in the experiment are presented by two vertical dashed lines. Solid vertical line represents wave number corresponding to Alfvén speed. Two horizontal dashed lines represent transverse wave numbers corresponding to $\lambda_\perp = 9\ cm$ and $\lambda_\perp = 18\ cm$.

In Fig. 9 the 3D current structures for left-handed polarization (Fig. 9(a)), single loop antenna (Fig. 9(b)), and right-handed polarization of the RMF source (Fig. 9(c)) are presented.

The picture features isosurfaces of the total current. The color shows the direction of the J_z component (red - J_z is positive, blue - J_z is negative). The black streamlines show the perturbed magnetic field in the planes perpendicular to the z-axis, which has two vortex structure.

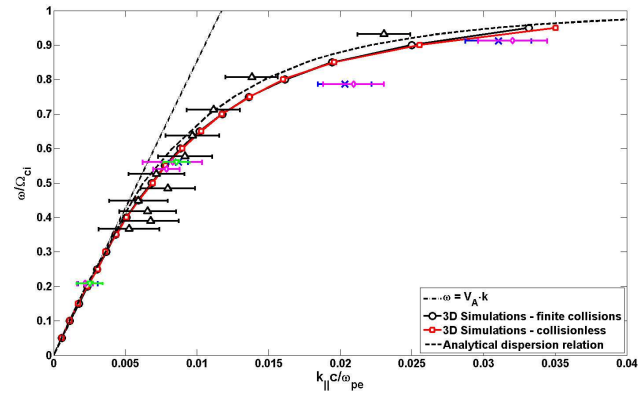

FIG. 7: (Color online) The RMF SAW dispersion relation obtained using 3D model for collisionless case (□) and the case with finite collisions given in the Table I (○). The analytical dispersion relation Eq. (1) is shown by dashed line. Experimental data: ▽ - one-loop antenna, × - right-hand polarization, ◇ - left-hand polarization, △ - reference[15].

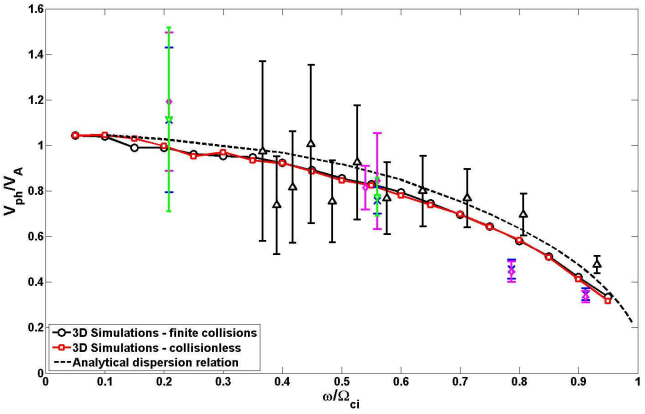

FIG. 8: (Color online) The RMF SAW phase velocity dependence on driving frequency obtained using 3D model for collisionless case (□) and the case with finite collisions given in the Table I (○). The analytical dispersion relation Eq. (1) is shown by dashed line. Experimental data: ▽ - one-loop antenna, × - right-hand polarization, ◇ - left-hand polarization, △ - reference[15].

The centers of the vortices correspond to the maxima of the current crossing the plane. For all the cases the current is very well confined by the ambient magnetic field. The current structure found in the 3D simulations is very similar to one found from the experimental measurements using $\mathbf{J} = c/(4\pi)\,\boldsymbol{\nabla} \times \mathbf{B}$ (See Fig. 9 in Ref.[15]).

D. Amplitude of perturbation as a function of frequency

In this section the dependence of the magnitude of the perturbed magnetic field on the driving frequency ω is discussed. In Fig. 10 the dependences measured in the experiment (◇) and calculated using the 3D model in collisionless and collisional cases for the experiment set 2 plasma parameters (See Table I) are presented. The currents in the loops are $I_1 = I_2 = 500$ *Amps*. One can see a very good agreement between the first four experimental points and the 3D model results. The dependence of the magnitude of the wave magnetic field measured in the the experiment and calculated using the 3D model is in a good agreement with another experiment performed in the LAPD[27]. In that experiment the SAWs were launched by a small (1 *cm* in diameter) circular copper mesh antenna and propagated in the varying along the axis of the machine background magnetic field, which is equivalent to varying ω/Ω_{ci} ratio.

The difference between the model and the experiment for the frequency $\omega = 0.93\Omega_{ci}$ can be explained by the following. As the driving frequency approaches the ion cyclotron frequency the ion resonant heating by the wave starts to play an important role and the wave transfers its energy to the ions. Besides that, because of the ion heating the SAW energy can be transferred also to another wave mode, namely, ion-acoustic wave, which propagates omnidirectionally unlike SAWs. This processes can lead to a dramatic decay of the wave magnitude and are not included in the 3D model. The last one can be included in the model by adding to the equation of motion of electrons (Eq. (A1c)) and ions (Eq. (A1d)) of $-\nabla p_e$ and $-\nabla p_i$ terms, respectively, where p_e and p_i are electron and ion pressures. The p_e and p_i are determined by the densities n_e and n_i through equations of states. Then the system of equations (A1) can be closed by including the continuity equations for electron and ion fluids.

For both the collisional and collisionless cases the SAW mode does not propagate above the ion cyclotron frequency, which explains the drop to zero of the 3D model curves for the frequencies higher than ion cyclotron frequency. The increase of the wave magnitude with the driving frequency can be explained by the fact that the parallel group velocity $v_g = \partial\omega/\partial k_{||}$ of the SAW, that is the wave energy propagation parallel to the ambient magnetic field, decays as the frequency increases (See Fig. 7). This means that the wave energy density and the wave magnitude increase. The maximum of the wave energy in the collisionless 3D model curve corresponds to the parallel wave length nearly matching the diameter of the antenna $D_a \approx \lambda_{||}/2$. The difference in the slopes of the collisional and collisionless 3D model curves is due to the dependences presented are for $z = 2.88$ *m* (Fig. 10), and the spatial decay rate along the ambient magnetic field due to collisions increase with frequency increasing.

E. Energy balance of the wave

The total energy generated by the RMF antenna which couples to the plasma wave is shared by four effects: the energy of the magnetic field $u_M = \frac{1}{2\mu_0} B_w^2$, energy of the electric field $u_E = \frac{1}{2}\varepsilon_0\varepsilon_\perp E_w^2$, and the kinetic energy of

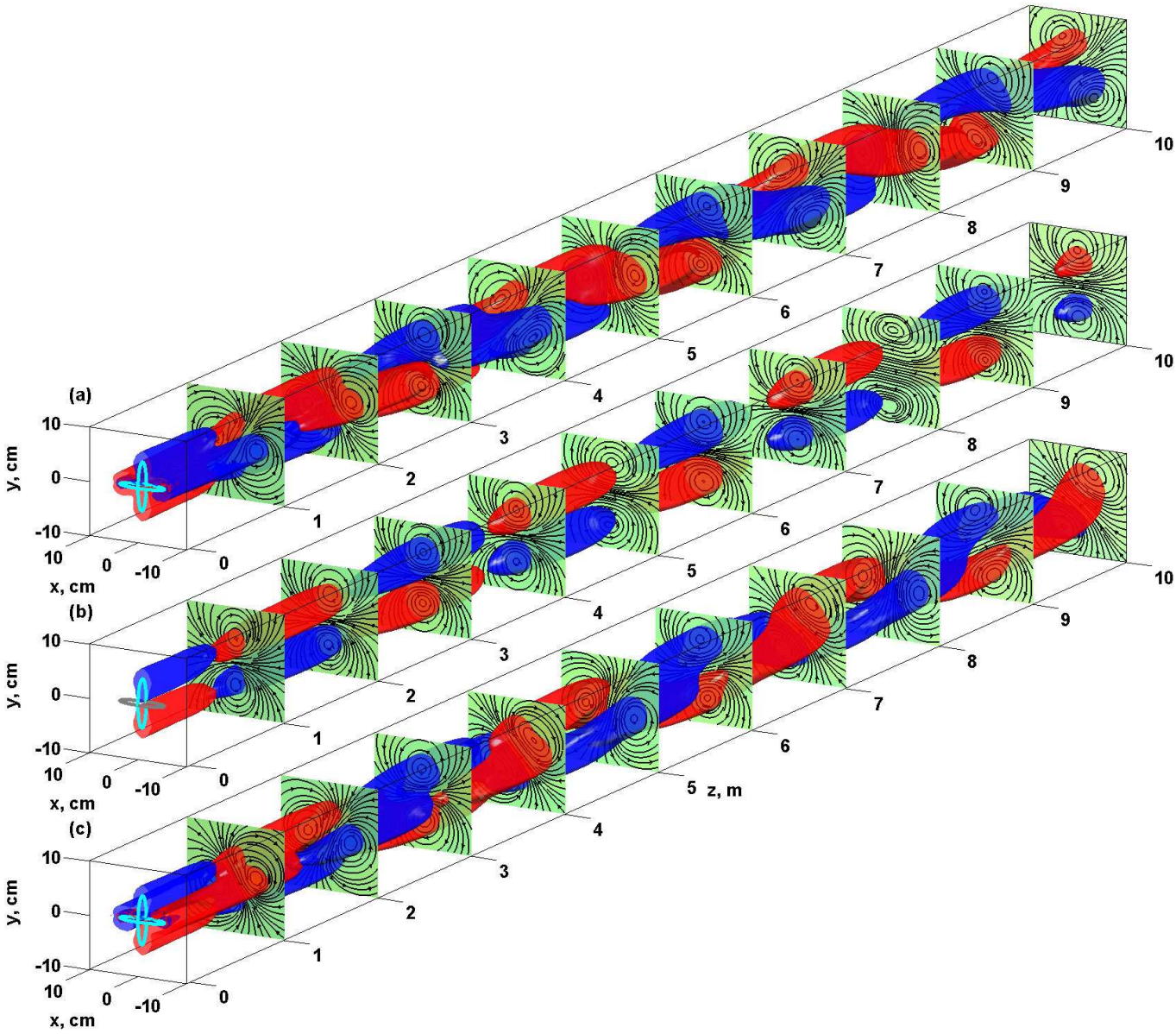

FIG. 9: (Color) Isosurfaces of total plasma current ($J = \sqrt{J_x^2 + J_y^2 + J_z^2}$) for the same time instant calculated using 3D model for left-hand polarization (a), one-loop antenna (b) (the current laying in xz-plane is turned off), and right-hand polarization cases (c). Red color corresponds to the isosurface with positive J_z-component of the plasma current, and blue - with negative J_z-component. The structures of the perturbed magnetic field in the planes perpendicular to z-axis are shown by black stream lines. The ambient magnetic field $B_0 = 1000\ Gauss$ is directed along z-axis. The radiating antenna is shown at the origin. Driving frequency $\omega = 0.54\Omega_{ci}$. Note that the length of the box shown is 10 m, and the size across z-axis is only 20 cm.

electrons u_{Ke}, and ions u_{Ki}. Here $\varepsilon_\perp$ is the perpendicular component of the plasma dielectric permittivity tensor, which is in general a function of plasma parameters and the wave frequency. To first order the magnetic and electric field components of the electromagnetic mode wave energy in the absence of charge separation are approximately equal. From the experimental measurements we can quite accurately derive the value of u_M. In Ref.[15] the wave magnetic field power was estimated as

$$P = V_A \frac{\delta B_w^2}{\mu_0} A, \tag{3}$$

where V_A is Alfvén speed δB_w is the magnitude of the perturbed magnetic field, and A is the characteristic cross section of the wave. The wave power for the Experiment set 1 estimated using Eq. (3) was $\sim 200\ W$. The wave power can be obtained more accurately using the Poynting vector crossing the plane perpendicular to the

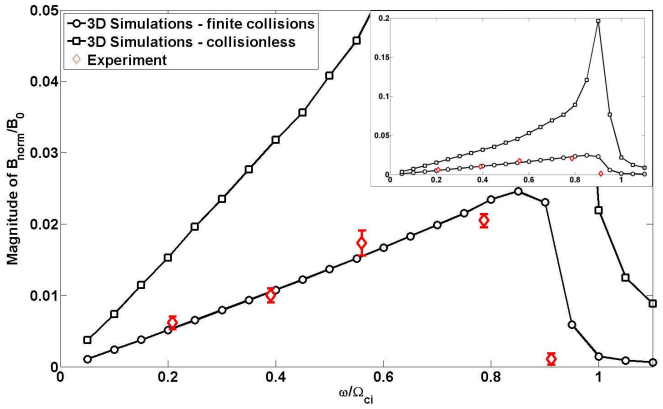

FIG. 10: Dependence of the magnitude of perturbed magnetic field at $z = 2.88\ m$ away from the antenna obtained using 3D model for collisionless case ($\square$) and the case with finite collisions ($\circ$) and measured in the experiment ($\diamond$) (Experiment set 2) for two-loop antenna case with left-hand polarization on the driving frequency. Magnitude of currents in the loops $I_1 = I_2 = 500\ Amps$. The large graph and the inset show the same dependences but with different scale on magnitude of B_{norm} axis.

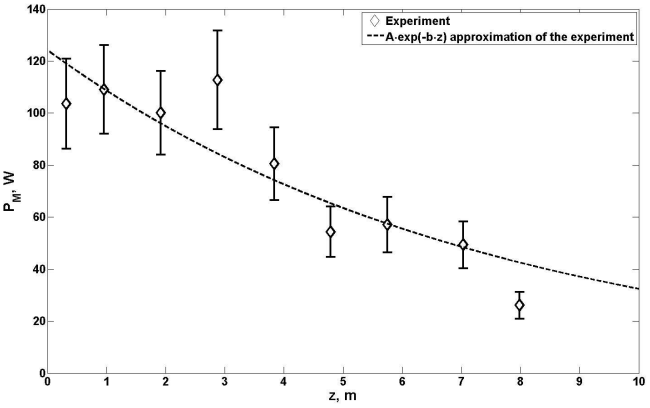

FIG. 11: Dependence of the magnetic component of the wave power propagating along the ambient magnetic field as a function of the distance from the antenna calculated from the experimental data ($\diamond$). Dashed line represent $A\exp(-bz)$ of the experimental points. (Experiment set 1, driving frequency $\omega = 0.54\Omega_{ci}$, magnitude of the currents $I_1 = I_2 \approx 600\ A$).

ambient magnetic field, given by

$$S = \frac{1}{2}\left(\varepsilon_0\varepsilon_\perp E_w^2 + \frac{1}{\mu_0}B_w^2\right)v_{g||} \approx \frac{1}{\mu_0}B_w^2 v_{g||}, \qquad (4)$$

where $v_{g||} = \frac{\partial\omega}{\partial k_{||}}$ is the parallel component of the wave group velocity. From Fig. 7 one can see that for the frequency $\omega = 0.54\Omega_{ci}$ the group velocity $v_{g||} \lesssim v_{ph||}$. Thus, the total energy passing trough the plane perpendicular to the ambient magnetic field per unit time is

$$P = \int \mathbf{S}d\mathbf{A} \approx \frac{v_{ph||}}{\mu_0}\int B_w^2 dA. \qquad (5)$$

The power calculated from the experimental data using Eq. (5) as a function of the distance from the antenna is presented in Fig. 11 as diamonds. the Dashed line in Fig. 11 represents the $A\exp(-bz)$ approximation of the experimental points. The exponential decay rate is determined by the collisions and is consistent with the exponential decay of the magnetic field magnitude (See Fig. 4). The antenna power which couples to the wave magnetic field is $2P_M\,(z=0) \approx 250\ W$ (2 is for the propagation in two directions along positive and negative z-directions) and the total electromagnetic energy of the wave is $\sim 500\ W$. There are no experimental measurements of the kinetic energies of the electrons and ions, except, it should be the same order as the magnetic field energy.

Using the 3D model we can calculate all components of the wave energy and the total power of the wave. The components of the wave energy as a function of time we calculate as

$$E_M(t) = \frac{1}{2\mu_0}\int_V |\mathbf{B}\,(t,x,y,z)|^2\,dV, \qquad (6a)$$

$$E_{Ke}(t) = \frac{nm_e}{2}\int_V |\mathbf{v}_e\,(t,x,y,z)|^2\,dV \qquad (6b)$$

$$E_{Ki}(t) = \frac{nm_i}{2}\int_V |\mathbf{v}_i\,(t,x,y,z)|^2\,dV \qquad (6c)$$

where V is the whole computational domain, n is the plasma density, m_e, m_i and $\mathbf{v}_e$ and $\mathbf{v}_i$ are electron and ion masses and velocities, respectively. Taking the time derivatives of Eqs. (6) we get the components of the power corresponding to the electric and magnetic fields and the electron and ion fluids. In the collisional case for a propagating mode there are no sinks of the energy in the model and the power injected by the antenna is equal to the sum of the wave power components.

In Fig. 12 the components of the wave energy as a functions of time for collisionless (Fig. 12(a)) and collisional (Fig. 12(b)) cases with experimental parameters (Experiment set 1) are shown. The time derivatives of the dependences of the energy components give the corresponding powers. From the 3D simulation in the collisionless case we found that the magnetic field power is $P_M = 253.0\ W$ (compared to $250\ W$ - the magnetic power estimated from the experimental data). The power which couples to the motion of ions is $P_{Ki} = 500.3\ W$, which is $1.98P_M$, and the power which couples to the motion of electrons is $P_{Ke} = 26.19\ W$. The total power radiated by the antenna in this case was found to be $\sim 1030\ W$ and during the $100\ \mu s$ pulse $103\ mJ$ is injected by the antenna. Thus, for the driving frequency $\omega = 0.54\Omega_{ci}$ the antenna power which couples to the wave is nearly equally distributed between the electromagnetic component and kinetic energy of ions, and the kinetic energy of electrons is of order $\sim 2.5\%$ of total wave energy.

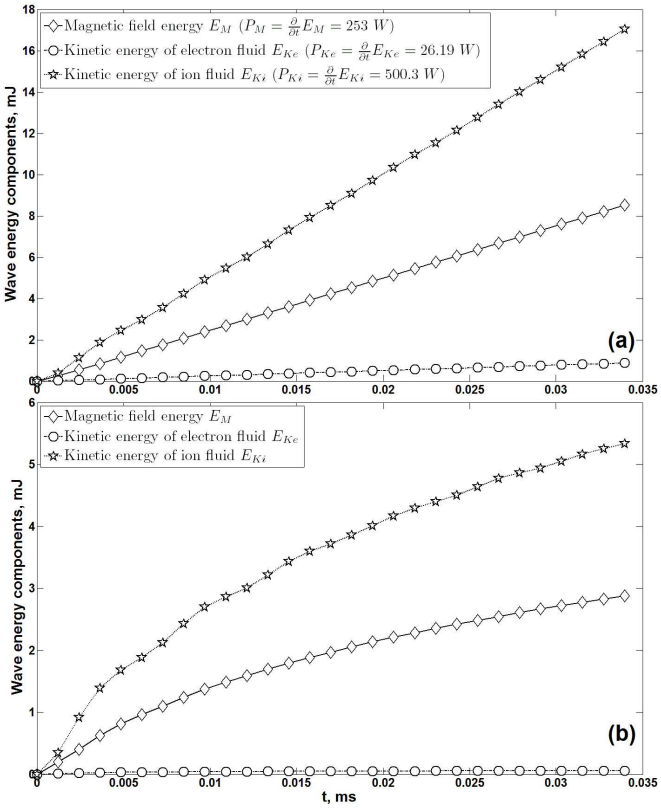

FIG. 12: Dependences of the components of the wave energy on time calculated using 3D model for collisionless (a) and collisional (b) cases. The time derivatives give the power corresponding to each component (Experiment set 1, driving frequency $\omega = 0.54\Omega_{ci}$, magnitude of the currents $I_1 = I_2 \approx 600\ A$).

In the collisionless case the wave energy grows linearly with time, as all energy injected by the antenna is conserved, while in the presence of the collisions the energy has a sink. This results in the decay of the time derivatives of the component energy dependencies with time. As the time progresses the propagating wave occupies larger volume, and larger parts of the ion and electron fluids are involved in motion. As a result the amount of energy lost due to the collisions increases. Asymptotically the wave comes to an energetic equilibrium with the media, when the power injected by the antenna is equal to the energy lost due to collisions per unit time.

IV. CONCLUSION

It is demonstrated in the experiments and three-dimensional cold two-fluid magnetohydrodynamics simulations that the rotating magnetic field antenna composed of two independent coils with alternating currents set $\pm 90^o$ out of phase can efficiently generate shear Alfvén waves with high transverse wave number with polarization depending on that of the RMF antenna. The results of semi-analytical 3D model simulations were compared with the measurements in the LAPD experiments and found to be in a good agreement for wide rage of the parameters.

The spatio-temporal wave structures calculated from the simulations are very close to those measured in the experiments. It is shown in the experiment[15] and calculated using the 3D model that the SAWs generated by the RMF carry significant field aligned currents which propagate parallel to the ambient magnetic field lines without noticeable spreading in the transverse direction.

The theoretical dispersion relation of the SAW, the dispersion relations calculated using 3D model and measured in the experiment are very close for a broad frequency range. The exponential decay rate of the wave along the ambient magnetic field is determined by the collisions.

The dependences of the magnitude of the wave magnetic field on the driving frequency measured in the experiment and calculated from 3D model are very close to each other except for the frequencies very close to the ion cyclotron frequency. This feature can be explained by the fact that the resonant wave-particle interaction and ion sound wave mode are not included in the model.

The power of the magnetic field of the generated wave is calculated from the experimental data (Experiment set 1) and found to be $\sim 250\ W$ for the driving frequency $\omega = 0.54\Omega_{ci}$, and the current magnitudes $I_1 = I_2 = 600\ A$. The power found in 3D simulations for the magnetic field power for the experimental parameters is $253\ W$, which differs from the experimental value only by $\sim 1\%$. The wave power corresponding to the other components of the wave, namely, the kinetic energy of electron and ion fluid calculated from 3D simulations are $P_{Ke} = 26.19\ W$, and $P_{Ki} = 500.3\ W$, respectively. Thus, the energy of the wave is distributed as: $\sim 1/2$ in the electromagnetic field energy, $\sim 1/2$ in the kinetic energy of ions, and $\sim 2.5\%$ in the kinetic energy of electrons. The fraction of the wave energy carried by the electrons gives an estimate of the error we would make for the experimental parameters if we considered the electrons as massless and modeled the plasma by a single-fluid MHD.

Thus, the 3D two-fluid MHD model was verified using the experimental results. Good overall agreement of the 3D model results with the experimental measurements for wide ranges of the experimental parameters shows good predictive capability of the 3D model, and it can be used for the parameters that are hard to achieve in laboratory plasmas or space plasmas.

Acknowledgments

The work was supported by ONR MURI grant No. N000140710789. The experiments were done on the Large Plasma Device (LAPD) at UCLA. The device is a part of the Basic Plasma Science Facility funded by the Department of Energy (Contract No. DE-FC02-

07ER54918) and the National Science Foundation (Contract No. NSF-PHY-0531621).

The authors thank Vipin K. Tripathi and Bengt Erik Eliasson for stimulating discussions on the magnitude dependences on driving frequency.

APPENDIX A: LINEAR TWO-FLUID MHD MODEL

In the Appendix we describe a linear 3D spectral model which was used to simulate the propagation of shear Alfvén waves generated by a RMF source. Following the EMHD approach[28–31], which was implemented into linear[14] and nonlinear[32] 3D EMHD spectral codes, we start form the Maxwell equations with the displacement current neglected. In the EMHD model the ions treated as motionless. While this approximation works fairly well for the frequency range well above the lower-hybrid resonance, it becomes unacceptable for the frequencies bellow ion cyclotron frequency Ω_{ci}, when the motion of ions become important in the wave propagation[33,34]. Thus, we can not consider the ions motionless.

On the other hand we would like the model to be able to produce valid results for broad frequency range including frequencies well above ion cyclotron frequency. In that case when the wave frequency approaches the lower-hybrid resonance frequency, we can not consider electrons as massless, as it is often done in single fluid MHD models. In order to satisfy both of the requirements we should consider the plasma as a media consisting of two cold fluids (electrons and ions) and resolve equation of motion for both of them.

The equations governing a quasineutral cold two-fluid plasma can be written as

$$\boldsymbol{\nabla}\times\mathbf{E} = -\frac{1}{c}\frac{\partial\mathbf{B}}{\partial t}, \tag{A1a}$$

$$\boldsymbol{\nabla}\times\mathbf{B} = \frac{4\pi}{c}\mathbf{J} + \frac{4\pi}{c}\mathbf{J}_{ext}, \tag{A1b}$$

$$\frac{\partial\mathbf{v}_e}{\partial t} + (\mathbf{v}_e\cdot\boldsymbol{\nabla})\,\mathbf{v}_e = -\frac{e}{m_e}\left(\mathbf{E}+\frac{1}{c}\mathbf{v}_e\times\mathbf{B}\right) - \nu_{en}\mathbf{v}_e - \nu_{ei}\left(\mathbf{v}_e - \mathbf{v}_i\right), \tag{A1c}$$

$$\frac{\partial\mathbf{v}_i}{\partial t} + (\mathbf{v}_i\cdot\boldsymbol{\nabla})\,\mathbf{v}_i = \frac{e}{m_i}\left(\mathbf{E}+\frac{1}{c}\mathbf{v}_i\times\mathbf{B}\right) - \nu_{in}\mathbf{v}_i - \nu_{ie}\left(\mathbf{v}_i - \mathbf{v}_e\right), \tag{A1d}$$

where indexes e and i denote electrons and ions, $\mathbf{J}$ is a plasma current, $\mathbf{J}_{ext}$ is an external current source, and ν_{en}, ν_{in}, ν_{ei}, and ν_{ie} are effective frequencies of collisions of electrons and ions with neutrals and Coulomb collisions. The last terms in Eqs. (A1c) and (A1d) correspond to momentum exchange between the electron and ion fluids due to Coulomb collisions. The conservation of the total momentum of two-fluid system requires that

$$\nu_{ie} = \frac{m_e}{m_i}\nu_{ei}. \tag{A2}$$

Let us decompose the total magnetic field as $\mathbf{B} = \mathbf{B}_0 + \mathbf{B}'$, where $\mathbf{B}_0$ is stationary uniform ambient magnetic field, and $\mathbf{B}'$ is the wave perturbation. The scales of the Eqs. (A1) are determined by two frequencies: electron plasma ω_{pe} and electron cyclotron Ω_{ce} frequencies. Normalizing length by the electron skin-depth $\lambda_e = c/\omega_{pe}$ and time by the inverse of electron cyclotron frequency $T = \Omega_{ce}^{-1}$, the dimensionless variable become $\bar{t} = t/T$, $\overline{\mathbf{x}} = \mathbf{x}/\lambda_e$, $\overline{\mathbf{v}} = T\mathbf{v}/\lambda_e$, $\overline{\mathbf{B}} = \mathbf{B}/B_0$, $\overline{\mathbf{E}} = (cT\mathbf{E})/(\lambda_e B_0)$ and $\overline{\nu} = \nu/\Omega_{ce}$.

Consider the case of small amplitude wave ($|\mathbf{B}'| \ll |\mathbf{B}_0|$). In that limit linearized Eqs. (A1) can be written in dimensionless form as

$$\overline{\boldsymbol{\nabla}}\times\overline{\mathbf{E}} = -\frac{\partial\overline{\mathbf{B}}}{\partial\bar{t}}, \tag{A3a}$$

$$\overline{\boldsymbol{\nabla}}\times\overline{\mathbf{B}} = \overline{\mathbf{v}}_i - \overline{\mathbf{v}}_e + 4\pi\overline{\mathbf{J}}_{ext}, \tag{A3b}$$

$$\frac{\partial\overline{\mathbf{v}}_e}{\partial\bar{t}} = -\left(\overline{\mathbf{E}} + \overline{\mathbf{v}}_e\times\mathbf{b}\right) - \overline{\nu}_{en}\overline{\mathbf{v}}_e - \overline{\nu}_{ei}\left(\overline{\mathbf{v}}_e - \overline{\mathbf{v}}_i\right), \tag{A3c}$$

$$\frac{\partial\overline{\mathbf{v}}_i}{\partial\bar{t}} = m_r\left(\overline{\mathbf{E}} + \overline{\mathbf{v}}_i\times\mathbf{b}\right) - \overline{\nu}_{in}\overline{\mathbf{v}}_i - m_r\overline{\nu}_{ei}\left(\overline{\mathbf{v}}_i - \overline{\mathbf{v}}_e\right), \tag{A3d}$$

where we neglected all nonlinear terms. m_r is the ratio between electron and ion masses ($m_r = m_e/m_i$), $\overline{\mathbf{B}}$ is dimensionless perturbed magnetic field and $\mathbf{b}$ is the unit vector in the direction of the ambient magnetic field $\mathbf{B}_0$, chosen to be along z-axis ($\mathbf{b} = \mathbf{e}_z$). We used also for the plasma current $\mathbf{J} = en\left(\mathbf{v}_i - \mathbf{v}_i\right)$, where for quasineutral plasma $n = n_e = n_i$. From this point to the end of the paper we will work only with dimensionless variable, so we drop the bars in the remaining section.

The external current $\mathbf{J}_{ext}$ entering Eq. (A3b), which is used to drive the RMF wave, can be introduced in the model as loops of an antenna. In the case of interest the size of the antenna is much smaller than the computational domain. That means that if we want to resolve the boundary problem on the current elements we have to use either nonuniform or very fine mesh with a large number of grid points. In the case of infinitely thin wires the current and the fields become singular. In order to avoid singularity in solution and remove the necessity to resolve boundary problem on the current elements we decompose the electric and magnetic field as $\mathbf{E} = \mathbf{E}' + \mathbf{E}_{ext}$ and $\mathbf{B} = \mathbf{B}' + \mathbf{B}_{ext}$, where

$$\mathbf{E}_{ext} = -\frac{\partial}{\partial t}\mathbf{A}_{ext}, \quad \mathbf{B}_{ext} = \boldsymbol{\nabla}\times\mathbf{A}_{ext}. \tag{A4}$$

Such decomposition can be chosen more or less arbitrary with the only requirement that the fields $\mathbf{E}_{ext}$ and $\mathbf{B}_{ext}$ have the same singularity at the vicinity of the external current as the total fields. One of the possible choices for the external vector potential $\mathbf{A}_{ext}$ is the screened potential satisfying the equation

$$\boldsymbol{\nabla}\times\boldsymbol{\nabla}\times\mathbf{A}_{ext} + (1+m_r)\,\mathbf{A}_{ext} = 4\pi\mathbf{J}_{ext}. \tag{A5}$$

The principle of superposition is applicable to the vector potential $\mathbf{A}_{ext}$, and it can be calculated for each current independently. If the current elements does not move in space and the time dependence appears only as $f(t)$ factor in $\mathbf{J}(\mathbf{x},t)$, the vector potential $\mathbf{A}_{ext}$ should be calculated only once at the very first time step. The ways of solving of Eq. (A5) for particular current configurations are described in Ref.[14,32].

Let introduce new variables:

$$\mathbf{V} = m_r \mathbf{v}_e + \mathbf{v}_i, \quad \mathbf{j} = \mathbf{v}_i - \mathbf{v}_e. \tag{A6}$$

which are the mass velocity of the two-component fluid up to the coefficient $(1+m_r)$ and the total current.

In these variables using Eqs. (A4),(A5) the system of Eqs. (A3) can be rewritten as

$$\boldsymbol{\nabla}\times\boldsymbol{\nabla}\times\mathbf{E}' = -\frac{\partial \mathbf{j}}{\partial t} - \frac{\partial}{\partial t}\mathbf{A}_{ext}, \tag{A7a}$$

$$\frac{\partial \mathbf{V}}{\partial t} = m_r \mathbf{j}\times\mathbf{e}_z + \alpha\mathbf{V} + \beta\mathbf{j}, \tag{A7b}$$

$$\frac{\partial \mathbf{j}}{\partial t} = (1+m_r)\,\mathbf{E}' + (\mathbf{V} - (1-m_r)\,\mathbf{j})\times\mathbf{e}_z + \\ + \gamma\mathbf{V} + \delta\mathbf{j} - (1+m_r)\frac{\partial}{\partial t}\mathbf{A}_{ext}, \tag{A7c}$$

where

$$\alpha = -\frac{\nu_{in} + m_r\nu_{en}}{1+m_r}, \tag{A8a}$$

$$\beta = m_r\gamma, \tag{A8b}$$

$$\gamma = \frac{\nu_{en} - \nu_{in}}{1+m_r}, \tag{A8c}$$

$$\delta = -\frac{(1+m_r)^2\nu_{ei} + \nu_{en} + m_r\nu_{in}}{1+m_r}. \tag{A8d}$$

All of these coefficients are just real number parameters depending on the effective collision rates and the electron/ion mass ratio.

Consider an arbitrary vector field $\mathbf{F}$ and its Fourier components $\mathbf{F}^*$. For any vector $\mathbf{F}$

$$\mathbf{k}\cdot(\mathbf{F}^*\times\mathbf{e}_z) = -i\left(\boldsymbol{\nabla}\times\mathbf{F}\right)^*_{||} = -iF^*_{c||}, \tag{A9}$$

where $F^*_{c||}$ is the Fourier component of the projection of $\boldsymbol{\nabla}\times\mathbf{F}$ on z-axis, that is parallel to the ambient magnetic field.

$$k_z F^*_z = -i\left(\boldsymbol{\nabla}\cdot\mathbf{F}_{||}\right)^* = -iF^*_{d||}, \tag{A10}$$

where $F^*_{d||}$ is the Fourier component of the divergence of the vector $\mathbf{F}$ component parallel to the ambient magnetic field.

$$\mathbf{k}\cdot\mathbf{F}^* - k_z F^*_z = -i\left(\boldsymbol{\nabla}\cdot\mathbf{F}_{\perp}\right)^* = -iF^*_{d\perp}, \tag{A11}$$

where $F^*_{d\perp}$ is the Fourier component of the divergence of the vector $\mathbf{F}$ component perpendicular to the ambient magnetic field.

Using definitions (A9), (A10), and (A11) Eqs. (A7) give in the Fourier domain

$$\frac{\partial}{\partial t}X = LX + S, \tag{A12}$$

where

$$X = \begin{bmatrix} j^*_{c||} \\ j^*_{d||} \\ V^*_{c||} \\ V^*_{d\perp} \\ C^* \end{bmatrix}, \quad S = -(1+m_r)\frac{\partial}{\partial t}\begin{bmatrix} A^*_{c||} \\ A^*_{d||} \\ 0 \\ 0 \\ 0 \end{bmatrix} \tag{A13}$$

and the system matrix

$$L = \begin{pmatrix} K\delta & -K(1-m_r) & K\gamma & -K & 0 \\ K_z(1-m_r) & K\delta & \frac{\gamma^2(K-2K_z)-K_z}{1+\gamma^2} & -\gamma\frac{\gamma^2 K+K_z}{1+\gamma^2} & \frac{\gamma^3(K-K_z)}{1+\gamma^2} \\ m_r\gamma & m_r & \alpha & 0 & 0 \\ m_r & -m_r\gamma & 0 & \alpha & 0 \\ 0 & 0 & 0 & 0 & \alpha \end{pmatrix}, \tag{A14}$$

where

$$C^* = V^*_{d\perp} - \frac{1}{\gamma}V^*_{c||} + \left(1+\frac{1}{\gamma^2}\right)V^*_{d||}. \tag{A15}$$

and

$$K = \frac{k^2}{1+m_r+k^2}, \quad K_z = \frac{k_z^2}{1+m_r+k^2}. \tag{A16}$$

Solution of Eq. (A12) can be written as[14,32]

$$X(\mathbf{k},t) = U(\mathbf{k})\,e^{\Lambda(\mathbf{k})t}U^{-1}(\mathbf{k})\,X(\mathbf{k},0) + \\ + U(\mathbf{k})\,e^{\Lambda(\mathbf{k})t}\int_0^t e^{-\Lambda(\mathbf{k})t'}U^{-1}(\mathbf{k})\,S(\mathbf{k},t')\,dt', \tag{A17}$$

where $\Lambda(\mathbf{k})$ and $U(\mathbf{k})$ are diagonal matrix of eigenvalues and modal matrix that consists of columns of corre-

sponding eigenvectors, which decompose the system matrix Eq. (A14) as

$$L = U\Lambda U^{-1} \tag{A18}$$

and do not depend on time. Thus, for a given geometry they can be computed for every $\mathbf{k}$ only once. Particularly, in the case of harmonically driven field and zero initial velocities of electron and ion fluids we get

$$S(\mathbf{k},t) = S(\mathbf{k})\, e^{-i\omega t}, \qquad X(\mathbf{k},0) = 0 \tag{A19}$$

and the solution (A17) become

$$X(\mathbf{k},t) = U(\mathbf{k})\, M(\mathbf{k},t)\, U^{-1}(\mathbf{k})\, S(\mathbf{k}), \tag{A20}$$

where

$$M(\mathbf{k},t) = \left(e^{\Lambda(\mathbf{k})t} - Ie^{-i\omega t}\right)\left(\Lambda(\mathbf{k}) + i\omega I\right)^{-1}, \tag{A21}$$

where I is identity matrix.

Thus, the problem reduces to finding eigen values and eigen vectors of the system matrix (A14) for every possible $\mathbf{k}$. To find the eigenvalues of $L(\mathbf{k})$ we need to solve characteristic equation which can be written in the form

$$(\alpha-\lambda)\begin{vmatrix} K\delta-\lambda & -K(1-m_r) & K\gamma & -K \\ K_z(1-m_r) & K\delta-\lambda & \frac{\gamma^2(K-2K_z)-K_z}{1+\gamma^2} & -\gamma\frac{\gamma^2K+K_z}{1+\gamma^2} \\ m_r\gamma & m_r & \alpha-\lambda & 0 \\ m_r & -m_r\gamma & 0 & \alpha-\lambda \end{vmatrix} = 0. \tag{A22}$$

If we replace λ by $-i\omega$ we will get the dispersion relation for the two-fluid system. The first term of the Eq. (A22) does not depend on $\mathbf{k}$ and describes the mode which is determined by electron-neutral and ion-neutral collision rates. The variable C^* (Eq. (A15)) depends only on the components of the mass velocity, and this mode is essentially a friction between the two-fluid system and neutral gas background. In the case of zero initial mass velocity this mode is not excited, and the variable C^* becomes an integral of motion and stays zero all the time.

The 4×4 determinant in Eq. (A22) gives in general case forth order equation for λ. All the coefficients of the equation are real. It means that the forth order equation has two pairs of complex conjugate roots. The real parts of the roots correspond to spatial decay rates, and the imaginary parts determine the wave propagation in $\pm$ directions with respect to the background magnetic field.

In the collisionless case ($\nu_{ei} = \nu_{en} = \nu_{in} = 0$) the 4×4 determinant in Eq. (A22) simplifies to the dispersion relation

$$\omega^4 - \left(m_r(K+K_z) + (1-m_r)^2 KK_z\right)\omega^2 + m_r^2 KK_z = 0. \tag{A23}$$

Introducing θ be the angle between the direction of the wave vector $\mathbf{k}$ and the ambient magnetic field ($k_z = k\cos\theta$), we get from Eq. (A23)

$$Ak^4 + Bk^2 + C = 0, \tag{A24}$$

where

$$A = \omega^4 + \cos^2\theta\left(m_r^2 - (1-m_r)^2\omega^2\right) - \tag{A25a}$$
$$- m_r\omega^2\left(1+cos^2\theta\right),$$
$$B = \omega^2(1+m_r)\left(2\omega^2 - m_r\left(1+cos^2\theta\right)\right), \tag{A25b}$$
$$C = \omega^4(1+m_r). \tag{A25c}$$

Note that the parameter $m_r < 10^{-4} \ll 1$ for, let say, He plasma, but during the derivation of the equations we did not neglected m_r compare to 1, so all the results are valid even for electron-positron plasma ($m_r = 1$). Since, we kept finite masses for both electrons and ions in the model described, it benefits in the ability of the model give valid results in the broad frequency range in different regimes: the Alfvén waves (below ion cyclotron frequency) and the whistler waves (well above the lower-hybrid resonance). As a matter of fact the EMHD model[14,28–32] is built in the two-fluid model as the limit $m_r \to 0$.

In Fig. 13 B_x component (perpendicular to the plane of the picture) of the perturbed magnetic field for different regimes calculated using described two-fluid MHD 3D model is presented in collisionless case. In Fig. 13(a) the wave generated with the driving frequency $\omega = 0.5\Omega_{ci}$ is presented. Note that in the Fig. 13(a) the scale along z-axis is 10 times larger than along y-direction. One can see that the wave generated is very well confined by the ambient magnetic field and the magnitude does not decay along z-axis, which are the properties of the Alfvén waves in collisionless plasmas. Unlike the Alfen wave regime the wave generated with frequency $\omega = 0.05\Omega_{ce}$ (See Fig. 13(b)) has cone structure and decay of the magnitude along z-axis due to spreading of the wave energy

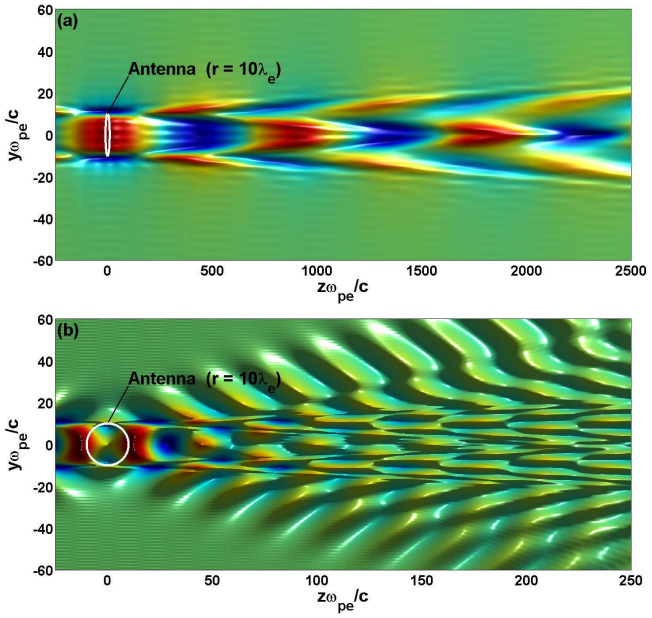

FIG. 13: (Color online) B_x component (perpendicular to the plane of the picture) of perturbed magnetic filed in the plane containing the loop with current (ring at the origin with radius $r = 10\lambda_e$) in different wave regimes calculated using two-fluid MHD 3D model in collisionless case: (a) - Alfvén wave ($\omega = 0.5\Omega_{ci}$), (b) - whistler wave ($\omega = 0.05\Omega_{ce}$).

inside the propagation cone, which is characteristic of whistler waves. For the frequency $\omega = 0.05\Omega_{ce}$ we compared the results of 3D two-fluid calculations with the results found using 3D EMHD model[14], and found that the relative difference between those has order of 10^{-4} for these parameters which is the order of m_r.

* Electronic address: karavaev@umd.edu

[1] W. Gekelman, J. Geophys. Res. **104**, 14417 (1999).
[2] I. de Pater and S. H. Brecht, Icarus **151**, 1 (2001).
[3] P. Louarn, J. E. Wahlund, T. Chust, H. de Feraudy, A. Roux, B. Holback, P. O. Dovner, A. I. Eriksson, , and G. Holmgren, Geophys. Res. Lett. **21**, 1847 (1994).
[4] J. Hollweg, M. Bird, H. Volland, P. Edenhofer, C. Stelzried, and B. Seidel, J. Geophys. Res. **87**, 1 (1982).
[5] A. Hasegawa, J. Geophys. Res. **81**, 5083 (1976).
[6] C. Goertz and R. Boswell, J. Geophys. Res. **84**, 7239 (1979).
[7] W. Gekelman, S. Vincena, D. Leneman, and J. Maggs, J. Geophys. Res. **102**, 7225 (1997).
[8] O. Alexandrova, A. Mangeney, M. Maksimovic, C. Lacombe, N. Cornilleau-Wehrlin, E. A. Lucek, P. M. E. Decreau, J.-M. Bosqued, P. Travnicek, and A. N. Fazakerley, J. Geophys. Res. **109**, A05207 (2004).
[9] C.-H. Hui and C. Seyler, J. Geophys. Res. **97**, 3953 (1992).
[10] D. Hayward and J. Dungey, Planet. Space Sci. **31**, 579 (1983).
[11] J. R. Wygant, A. Keiling, C. A. Cattell, M. Johnson, R. L. Lysak, M. Temerin, F. S. Mozer, C. A. Kletzing, J. D. Scudder, W. Peterson, et al., J. Geophys. Res. **105**, 18675 (2000).
[12] Y. Yasaka, R. Majeski, J. Browning, N. Hershkowitz, and D. Roberts, Nucl. Fusion **28**, 1765 (1988).
[13] D. R. Roberts, N. Hershkowitz, R. Majeski, and D. H. Edgell, AIP Conf. Proc. **190**, 462 (1989).
[14] A. V. Karavaev, N. A. Gumerov, K. Papadopoulos, X. Shao, A. S. Sharma, W. Gekelman, A. Gigliotti, P. Pribyl, and S. Vincena, Phys. of Plasmas **17**, 012102 (2010).
[15] A. Gigliotti, W. Gekelman, P. Pribyl, S. Vincena, A. Karavaev, X. Shao, A. S. Sharma, and D. Papadopoulos, Phys. of Plamas **16**, 092106 (2009).
[16] W. Gekelman, H. Pfister, Z. Lucky, J. Bamber, D. Leneman, and J. E. Maggs, Rev. Sci. Instrum. **62**, 2875 (1991).
[17] P. Baille, J.-S. Chang, A. Claude, R. M. Hobson, G. L. Ogram, and A. W. Yau, J. Phys. B: At. Mol. Phys. **14**, 1485 (1981).
[18] J. M. Anderson and L. Goldstein, Phys. Rev. **100**, 1037 (1955).
[19] E. T. Everson, P. Pribyl, C. G. Constantin, A. Zylstra, D. Schaeffer, N. L. Kugland, and C. Niemann, Rev. Sci. Instrum. **80**, 113505 (2009).
[20] T. Drozdenko and G. J. Morales, Phys. Plasmas **8**, 3265 (2001).
[21] G. J. Morales and J. E. Maggs, Phys. of Plasmas **4**, 4118 (1997).
[22] W. Gekelman, S. Vincena, and D. Leneman, Plasma Physics and Controlled Fusion **39**, A101 (1997).
[23] W. Gekelman, S. Vincena, N. Palmer, P. Pribyl, D. Leneman, C. Mitchell, and J. Maggs, Plasma Physics and Controlled Fusion **42**, B15 (2000).
[24] J. Vranjes, D. Petrovic, S. Poedts, M. Kono, and V. M. Cadez, Planet. Space Sci. **54**, 641 (2006).
[25] G. J. Morales, R. S. Loritsch, and J. E. Maggs, Phys. of Plasmas **1**, 3765 (1994).
[26] W. Gekelman, D. Leneman, J. Maggs, and S. Vincena, Phys. of Plasmas **1**, 3775 (1994).

[27] S. Vincena, W. Gekelman, and J. Maggs, Phys. Plasmas **8**, 3884 (2001).
[28] A. V. Streltsov, M. Lampe, W. Menheimer, G. Ganguli, and G. Joyce, J. Geophys. Res. **111**, A03216 (2006).
[29] A. S. Kingsep, K. V. Chukbar, and V. V. Yankov, Rev. Plasma Phys. **16**, 243 (1990).
[30] A. V. Gordeev, A. S. Kingsep, and L. I. Rudakov, Phys. Rep. p. 243 (1994).
[31] M. Lampe, G. Joyce, W. M. Manheimer, A. Streltsov, and G. Ganguli, J. of Comp. Phys. **214**, 284 (2006).
[32] N. A. Gumerov, A. V. Karavaev, A. S. Sharma, X. Shao, and K. D. Papadopoulos, Efficient spectral and pseudospectral algorithms for 3D simulations of waves in plasmas, Submitted to J. of Comp. Phys. (2010).
[33] T. N. C. Wang and T. F. Bell, Rev. de Physique Appliquee **7**, 11 (1972).
[34] I. G. Kondrat'ev, A. V. Kudrin, and T. M. Zaboronkova, Radio Sci. **27**, 315 (1991).